Volume 1 | Number 1 | Jan 2013 | Pages 1–100

Nanoscale

www.rsc.org/nanoscale

ROYAL SOCIETY OF CHEMISTRY

ROYAL SOCIETY OF CHEMISTRY

www.rsc.org/nanoscale

1   # The role of amorphous precursors in the

2   # crystallization of La and Nd carbonates

3

4 Beatriz Vallina[a,*], Juan Diego Rodriguez-Blanco[a,b], Andrew P. Brown[c], Jesus A.

5 Blanco[d], Liane G. Benning[a,e,*]

6

7 [a] School of Earth and Environment, University of Leeds, Leeds LS2 9JT, UK

8 [b] Nano-Science Center; Department of Chemistry; University of Copenhagen H.C. Oersted Institute, C Bygn, 9

9 Universitetsparken 5, DK 2100 Copenhagen, Denmark

10 [c] Institute for Materials Research, SCaPE, Faculty of Engineering. University of Leeds, LS2 9JT, UK.

11 [d] Departamento de Física, Universidad de Oviedo, Oviedo, E-33007, Spain

12 [e] Research Center for Geosciences, GFZ, Interface Geochemistry Section, 14473, Potsdam, Germany.

13 * e-mail: earbv@leeds.ac.uk; l.g.benning@leeds.ac.uk

14

17

18

19

20

21

22 SENTENCE HIGHLIGHTING THE NOVELTY OF THE WORK (MAX. 20 WORDS)

23 Rare-earth carbonates form from nanoparticulate metastable poorly-ordered
24 precursors with highly variable lifetimes and crystallization pathways depending on
25 composition and temperature.

26

27

28   **ABSTRACT**

29

30   Crystalline La and Nd carbonates can form from poorly-ordered nanoparticulate

31   precursors, termed amorphous lanthanum carbonate (ALC) and amorphous

32   neodymium carbonate (ANC). When reacted in air or in aqueous solutions these

33   precursors show highly variable lifetimes and crystallization pathways. We have

34   characterized these precursors and the crystallization pathways and products with

35   solid-state, spectroscopic and microscopic techniques to explain the differences in

36   crystallization mechanisms between the La and Nd system. ALC and ANC consist of

37   highly hydrated, 10-20 nm spherical nanoparticles with optimal formulas of

38    $REE_2(CO_3)_3 \cdot 5H_2O$ (REE=La, Nd). The stabilities differ by $\sim$ 2 orders of magnitude,

39   with ANC being far more stable than ALC. This difference is due to the Nd^{3+} ion

40   having a far higher hydration energy compared to the La^{3+} ion. This, together with

41   temperature and reaction times, lead to clear differences in the kinetics and

42   mechanisms of crystallization of the amorphous precursor La- and Nd-carbonate

43   phases but also in the resulting crystallite sizes and morphologies of the end products.

44   All crystalline La and Nd carbonates developed spherulitic morphologies when

45   crystallization occurred from hydrous phases in solution at temperatures above 60 °C

46   (La system) and 95 °C (Nd system). We suggest that spherulitic growth occurs due to

47   a rapid breakdown of the amorphous precursors and a concurrent rapid increases in

48   supersaturation levels in the aqueous solution. The kinetic data show that the

49   crystallization pathway for both La and Nd carbonate systems is dependent on

50   reaction temperature and the ionic potential of the REE^{3+} ion.

51

52

53

54   **1. INTRODUCTION**

55

56   The formation of crystalline carbonates from supersaturated solutions often

57   starts with the precipitation of a phase made of nanoparticles with diameters smaller

58   than 100 nm, and which when characterized with conventional X-ray diffraction show

59   an amorphous character.[1-4] These amorphous precursors are usually unstable and

60   sometimes transform to nanocrystalline, often metastable intermediate phases prior to

61   the transformation into thermodynamically stable end products.[5] However, such

62   amorphous precursors can also remain stable and not crystallize for long time periods

63   (days-years; e.g., phosphates or amorphous silica.[6-7] When they are highly unstable

64   (seconds to minutes) they are difficult to detect with conventional techniques because

65   of the short lifetimes.[8-10]

66   Most of the in-depth research on the formation and stability of amorphous

67   precursors has focused on mineral systems that are key in biomineralization

68   processes, (e.g., amorphous Ca-Mg carbonates[4,5,11-14] or amorphous Ca

69   phosphates[15,16]). However, the search of potential materials for specialized industrial

70   applications has recently also brought attention to the formation and stability of

71   amorphous rare-earth element (REE) carbonate phases[17-19] and the corresponding

72   crystalline end products.

73   REEs are moderately abundant in the Earth's crust, but they are not

74   concentrated enough to make them easily exploitable economically. The most

75   important REE source in the world is the Bayan Obo deposit, China, where more than

76   90% of world's REE raw materials are extracted,[20] and relatively high concentrations

77   of REE have also been found in deep-sea ferromanganese nodules.[21] Two of the most

78   important REEs are lanthanum (La) and neodymium (Nd) and both belong to the

79   Light Rare Earth Elements group (LREE), which tend to concentrate in carbonates

80   and phosphates in 8- to 10-fold coordination.[22,23] La and Nd have similar f-electron

81   configurations and their ionic radii only differ by 0.07 Å (R_{La}=1.15 Å; R_{Nd}=1.08 Å;

82   ionic potentials of 2.60 and 2.78 Å^{-1}, respectively[24-26]). La is the most abundant

83   trivalent REE with diverse industrial and technological applications including

84   metallurgy,[27] fluorescent biological labels,[28] pollution control catalysts,[18,20] gas

85   sensors and CO_2 absorbing ceramics.[29] While, Nd is an essential additive in

86   neodymium-iron-boron ($Nd_2Fe_{14}B$) permanent magnets that are crucial in consumer

87   electronics, energy materials, defence applications[18,19] and is a key component of

88   many lasers.[30] Furthermore, Nd is an important component in glass technologies[31] and

89   geochronological rock dating.[20]

90   In the last decade or so the supply of La and Nd for all these applications has

91   become constrained while demand for a variety of new technologies has grown.[20]

92   According to the US Department of Energy,[17] La has been classified as a near-critical

93   REE, while Nd has been identified as one of the most critically needed REEs together

94   with dysprosium, europium, terbium and yttrium. This classification is based on a

95   balance between the importance of REEs for the development of clean energy and the

96   supply of such REEs in the short (present-2020) and medium (2015-2025) terms. This

97   increasing demand has driven the study of the origin and distribution of REEs in

98   carbonate deposits. However, there is lack of basic data regarding the mechanisms of

99   crystallization of REE-bearing carbonates and, in particular, the first stages of

100   formation.

101   Different natural or synthetic REE-bearing carbonates are known. These

102   include the REE carbonates lanthanite $[REE_2(CO_3)_3 \cdot 8H_2O]$, tengerite $[REE_2(CO_3)_3 \cdot 2$-

103   $3H_2O]$, hydroxylbastnasite $[REECO_3(OH)]$, and kozoite $[REECO_3(OH)]$, as well as

104   several REE-bearing oxide carbonates $(REE_2O_2CO_3)$. The major REE carbonates

105   occurring in natural REE deposits also contain F^- as well as OH^- in their structures

106   (see references in Table SI-1). Many studies have addressed the crystalline products

107   of the synthesis of REE carbonates from aqueous solutions as a function of

108   crystallization temperature, pressure, nature and concentrations of reagents or

109   stirring.[32-34] Furthermore, some studies have focused on the effect of the ionic radii of

110   different REEs on the crystal structure of the crystalline product.[33,35] However,

111   information about the early stages of the precipitation reactions and the role that

112   amorphous precursors or metastable intermediates may play in the crystallization

113   pathways is surprisingly scarce. Recently, we have shown[36] that dysprosium (Dy)

114   carbonates form via the crystallization of a highly hydrated amorphous precursor

115   (amorphous dysprosium carbonate, $Dy_2(CO_3)_3 \cdot 4H_2O$). A few studies mention the

116   formation of amorphous lanthanum[37,38] and neodymium carbonates[39-42] during the

117   initial stages of precipitation, but the composition, basic characteristics or stability of

118   these La or Nd amorphous phases as well as the subsequent crystallization pathways

119   have so far not been addressed. Thus, we still lack information about the factors that

120   affect the stability of these amorphous precursors and whether the degree of hydration

121   or the kinetics of dehydration and crystallization of all amorphous REE carbonates is

122   similar.

123   To address this, we have carried out a study on the formation and

124   crystallization of La and Nd carbonates from aqueous solution. We have characterized

125   the first formed phases and followed their transformation to crystalline REE

126   carbonates both in air and in solution over a range of temperatures (25-220 ºC) and

127   reaction times (minutes to many months). The data reveal that the amorphous La and

128   Nd carbonate precursors have temperature-dependent stabilities and that depending on

129   reaction conditions the crystallization of REE-bearing carbonates proceeds via

130   spherulitic growth and / or via dissolution-re-precipitation. Finally, the kinetic data

131   revealed crystallization pathways that were primarily dependent on the ionic potential

132   of the REE and the reaction temperature.

133

134

135   **2. EXPERIMENTAL**

136

137   Lanthanum and neodymium carbonates were obtained by mixing a solution of

138   $La(NO_3)_3 \cdot 6H_2O$ (10 mM, Alfa Aesar, 99.9% purity) or $Nd(NO_3)_3 \cdot 6H_2O$ (10 mM, Alfa

139   Aesar, 99.9% purity) with a Na_2CO_3 solution (10 mM, Fisher Scientific, 99.9%

140   purity). Experiments were carried out at room temperature (21 ºC) under constant and

141   continuous stirring. Immediately after mixing a white (La-system) or pink (Nd-

142   system) precipitate formed. Aliquots of these precipitates were treated using four

143   different approaches. One batch was kept dry at ambient conditions (hereafter these

144   experiments are termed *dry-ambient*) and analyses for up to 6 months by X-ray

145   diffraction (see below) to assess whether or not they crystallized. A second dry batch

146   was reacted in air at temperatures between 25 and 1000 ˚C. Changes in the properties

147   of this dried, initial precipitate (i.e., its crystallization) were monitored using

148   thermodiffraction (termed: *dry-heated*). The final two batches were aged in the native

149   solution either at 21 °C for up to two months (*wet-ambient*), or hydrothermally at 60,

150   95, 165 and 220 °C for up to 7 days (*hydrothermal*). The hydrothermal treatments

151   were carried out in Teflon-lined stainless steel (40 mL) vessels at saturated water

152   vapour pressures. Both the *wet-ambient* and *hydrothermal* suspensions were shaken

153   regularly. All experiments were repeated a mininum of three and a maximum of six

154   times.

155   The initial precipitates, various intermediate products as well as the reaction

156   products at the end of each treatment were quenched to room temperature and vacuum

157   filtered through 0.2 μm polycarbonate membranes where required. The resulting

158   solids were washed with water and isopropanol following the method described in

159   Rodriguez-Blanco et al. (2008).[4] All solid phases were characterized by powder X-ray

160   diffraction (XRD), Fourier transform infrared spectroscopy (FTIR), and scanning

161   electron microscopy (SEM). The dried initial precipitates were also characterized by

162   thermogravimetric analyses (TGA) and high-resolution transmission electron

163   microscopy (HR-TEM), and crystallization was followed by time- and temperature-

164   resolved powder X-ray thermodiffraction (XRTD).

165   Conventional powder XRD patterns were collected using a Bruker D8 powder

166   X-ray diffractometer (CuKα_1; 2θ range 10-75; 0.005°/step and 0.1 s/step), while

167   powder XRTD was carried out in air using a Panalytical X´Pert Pro diffractometer

168   equipped with an Anton Paar HTK 1200N High-Temperature Oven-Chamber

169   (CuK$\alpha_{1,2}$; 2θ range 20-50 at 0.01°/step and 0.16 s/step; constant heating rate of 1

170   °C/min from 25 to 1000 °C). Crystallite sizes were calculated from the diffraction

171   patterns using the Scherrer equation,[43] with the assumption that the particles were

172   stress-free and with pattern-matching refinement of the crystalline phases carried out

173   using the Rietveld refinement software TOPAS.[44] Furthermore, all crystallite sizes

174   were calculated taking into account the instrumental line-broadening of the

175   diffractometer by using an X-ray pattern of a silicon standard (2θ_{111}= 28.46° and

176   FWHM= 0.049°). FTIR spectra were recorded on an A2-Technology Microlab

177   Portable mid-IR spectrometer with a Diamond internal reflection cell (DATR). The

178   spectra were collected by adding 1024 scans in the 650-4000 cm^{-1} range at a

179   resolution of 4 cm^{-1}. Themogravimetric analyses (TGA) were carried out with a

180   Mettler TA 4000 instrument, while heating the samples from 25 to 1000 °C at a rate

181   of 10 °C/min in a N$_2$ atmosphere. Images of the solids were acquired by field

182   emission gun scanning electron microscopy (FEG-SEM, LEO 1530 Gemini, operated

183   at 3 kV and with an in-lens detector, equipped with an Oxford Instruments energy-

184   dispersive X-ray (EDX) analysis system; Isis) and by FEG-transmission electron

185   microscopy (FEG-TEM: FEI CM200; operated at 197 kV and equipped with an

186   Oxford Instruments energy-dispersive X-ray (EDX) analysis system (Isis) and a Gatan

187   Imaging Filter (GIF-200)).

188   In addition, we carried out turbidity experiments by mixing a solution of

189   La(NO$_3$)$_3$·6H$_2$O or Nd(NO$_3$)$_3$·6H$_2$O (10 mM) with a solution of Na$_2$CO$_3$ (10 mM) in a

190   cuvette inside a stirred module of a double beam UV-VIS spectrophotometer (Uvikon

191   XL, SECOMAN Ltd). The development of turbidity was followed *in situ* and in a

192   time-resolved manner by changes in UV-VIS spectra recorded at a wavelength of 450

193   nm every second for up to 17 hours to assess the formation and real time

194   transformation of the initial precipitates.

195   Lastly, the saturation indexes (SI) of lanthanites (both La and Nd forms) in the

196   initial solutions and prior to the formation of the first precipitates were calculated with

197   the geochemical code PHREEQC[45] using the only available solubility products for

198   lanthanite-(La or Nd) in the literature.[46] The saturation index is defined as:

199

200   $$SI = \log \frac{IAP}{K_{sp}}$$ [1]

201

202   where *IAP* corresponds to the ion activity product in solution and K_{sp} is the solubility

203   product of the solid phase.

204

205

206

207   **3. RESULTS**

208   **3.1. The initial La and Nd precipitates and crystallisation under dry**

209   **conditions.**

210   Upon mixing of the $La(NO_3)_3 \cdot 6H_2O$ or $Nd(NO_3)_3 \cdot 6H_2O$ and Na_2CO_3 starting

211   solutions white (La) and pink (Nd) precipitates formed respectively. The X-ray

212   patterns of these precipitates were quite similar, showing only three humps centred at

213   ~ 15-20, 30 and 45º 2θ (marked with * in the Fig. 1 a and b, bottom patterns)

214   indicating the presence of solely amorphous materials in both systems. Interestingly,

215   both these amorphous phases remained stable when stored in a dry state in air (*dry-*

216   *ambient*; Table 1), but the lifetimes were very different. The La-bearing amorphous

217   phase stored in a dry state remained stable for ~ 48 hours before crystallizing to

218   lanthanite-(La) $[La_2(CO_3)_3 \cdot 8H_2O]$, ICSD-22224,[47] while the dry Nd-bearing

219   amorphous phase remained stable for up to 6 months. When *dry-heated* between 25

220   °C and 1000 °C with simultaneous recording of thermodiffraction patterns these

221   amorphous phases behaved significantly different. The amorphous La-bearing

222   precursor remained amorphous when heated up to 400 ºC (lower patterns in Fig. 1a)

223   and only at 450 ºC did it start to transform to a crystalline compound identified as

224   monoclinic La-dioxycarbonate ($La_2O_2CO_3$; patterns at 450 ad 550 °C in Fig. 1a,

225 ICDD PDF2 048-1113). Upon further heating to 700 ºC this monoclinic La-
226 dioxycarbonate transformed to hexagonal La-dioxycarbonate ($La_2O_2CO_3$; ICCD
227 PDF2 037-0804; pattern at 700 °C, Fig. 1a). Above 700 ºC the hexagonal La-
228 dioxycarbonate transformed to hexagonal La-oxide (La_2O_3; ICCD PDF2 005-0602),
229 which remained the sole phase present between 800 to 1000 ºC (Fig. 1a, upper
230 pattern). In the case of the amorphous Nd-bearing phase, the thermodiffraction
231 patterns revealed no Bragg peaks up to 450 ºC (Lower 3 patterns in Fig. 1b). By 550
232 ºC the amorphous carbonate precursor transformed to monoclinic Nd-dioxycarbonate
233 ($Nd_2O_2CO_3$; Fig. 1b, pattern at 550 °C, ICCD PDF2 023-0421), at 700 ºC (Fig. 1b,
234 pattern at 700 °C) to cubic Nd-oxide (Nd_2O_3; ICCD PDF2 03-065-3184) and at 800
235 ºC, the cubic Nd-oxide had transformed to hexagonal Nd-oxide (Nd_2O_3; Fig. 1b,
236 upper pattern; ICCD PDF2 041-1089). This latter phase remained the only phase in all
237 patterns up to 1000 °C.

238 The amorphous nature of both precursor materials identified by XRD was
239 confirmed by high-resolution TEM. The images of these pristine phases revealed
240 roughly spherical nanoparticles with diameters between 10 and 20 nm (Fig. 2a) that
241 show no crystallinity by selected area electron diffraction (data not shown).
242 Standardless quantification of EDX spectra (inset in Fig. 2a) from these amorphous
243 nanoparticles revealed a La:O atomic ratio of ∼ 2:8. The particles rapidly crystallized
244 when exposed to the electron beam of the TEM for a few seconds, resulting in
245 nanocrystals with interplanar spacing of ∼ 2.9 Å (Fig. 2b). This value corresponds to
246 the (101) d-spacing of hexagonal La-oxide (La_2O_3; ICCD PDF2 005-0602). The
247 crystallization of the amorphous starting material to hexagonal La-oxide was also
248 confirmed by quantification from EDX spectra, which showed a decrease in the
249 amount of O from ∼ 2:8 La:O ratio in the amorphous precursor to ∼ 2:3 La:O ratio in
250 La_2O_3. A similar behaviour was found for the Nd precursor material. High-resolution
251 TEM images of the pristine Nd precursor showed no significant differences in
252 morphology compared to the La bearing phase (Fig. 2c) and the electron beam also
253 crystallized the initial nanoparticles after a few seconds of exposure. The newly
254 formed nanocrystals showed an interplanar spacing of ∼ 3.2 Å (Fig. 2d), which
255 matched with the (222) d-spacing of cubic Nd-oxide (Nd_2O_3; ICCD PDF2 03-065-
256 3184). EDX spectra from the neodymium amorphous precursor and cubic Nd-oxide

257   showed the same Nd:O ratios as those obtained in the experiment with La (i.e. ~ 2:8

258   and ~ 2:3, before and after significant electron beam exposure respectively).

259   The FTIR analysis of the amorphous La and Nd phases revealed identical

260   ionic vibrations. Both spectra are characterized by typical carbonate and O-H

261   vibrations (Fig. 3, lower and upper spectra correspond to amorphous La and Nd

262   carbonate, respectively). The broad band between ~ 2500 and 3700 cm^{-1} (marked as

263   band 1; detailed assignments see Table SI-2) represents O-H stretching vibrations and

264   corresponds to structural water. The most intense vibrations in both precursors were

265   located between ~ 1455 and 679 cm^{-1} (bands 2-8) and are characteristic of the main

266   stretching   vibrations   of   the   carbonate   ions.   Combined   with   the   X-ray

267   thermodiffraction results (Fig. 1), this confirms that both La and Nd precursors are

268   amorphous and strongly hydrated La and Nd carbonates. These phases will for

269   simplicity hereafter be called ALC and ANC respectively, in line with other

270   amorphous   carbonates   in   the   literature   (e.g.,   amorphous   calcium   carbonate,

271   ACC[4,11,48]).

272   Thermogravimetric analyses (Fig. 4a, b) show that upon gradual heating the

273   total weight loss of ALC and ANC was ~ 40%. For ALC, ~ 16% of the total weight

274   loss corresponds to the release of water at ~ 100 ºC (corresponding to the equivalent

275   of five water molecules per formula unit [pfu]), while the remaining 23% mass loss

276   was due to the decomposition of the carbonate at about 450 ºC and its full

277   transformation to hexagonal La-oxide above ~ 700 ºC. The dehydration and

278   decarbonation processes of both amorphous precursors followed the same steps.

279   However, in the case of ANC, the small weight loss above ~ 700 ºC (~ 1%) was

280   slower and more progressive compared to ALC (Fig. 4).

281

282   **3.2. Crystallization of ALC and ANC in aqueous solution**

283   Compared to the dry conditions, the behaviour of ALC and ANC was

284   completely different when reacted in the solutions in which they were initially formed

285   (either under *wet-ambient* or *hydrothermal* conditions). Both ALC and ANC

286   crystallized much faster compared to the dry conditions. Their crystallization also

287   followed different pathways that were dependent on composition, temperature and

288   reaction times (Table 1 and 2).

289   At ambient conditions the development of turbidity in both systems when
290 followed by *in situ* and time resolved UV-Vis spectra (Fig. 5) revealed that in the
291 ALC case, after ~ 2 minutes the turbidity started to increase as a consequence of the
292 progressive transformation of ALC to crystalline La carbonate phases. The
293 absorbance reached a maximum value after 8 minutes, indicating the completion of
294 the crystallization reaction. The subsequent decrease in turbidity is most probably a
295 consequence of sedimentation of the crystalline particles. The end products of these
296 experiments (Fig. 6a, bottom pattern; Table 1) were identified by XRD as the highly
297 hydrated but crystalline lanthanite-(La) [$La_2(CO_3)_3·8H_2O$; ICSD-22224[47]).
298 Conversely, ANC, which also formed immediately after mixing, remained stable for
299 more than ~2 hours before it started to crystallize and its crystallization took ~15
300 hours. The end product was also identified as a lanthanite-(Nd) ([$Nd_2(CO_3)_3·8H_2O$];
301 Fig. 6b, bottom pattern; Table 1). In both systems after 60 days at ambient
302 temperature these lanthanite octahydrates recrystallized and transformed to kozoite-
303 (La) [$LaCO_3(OH)$] (ICSD 6180) in the La system, while in the Nd system, ~ 90% of
304 the initial lanthanite-(Nd) transformed to tengerite-(Nd) [$Nd_2(CO_3)_3·2-3H_2O$] (ICSD
305 1554; Fig. 6b; Table 2).

306   When the transformation was carried out also in aqueous media but at 60 ºC
307 (*hydrothermal*), ALC showed a similar behaviour as at 21 ºC. After 4 hours
308 lanthanite-(La) was the only phase detected (Fig. 6a, lower pattern, Table 1), after 24
309 hours ~40 % transformed to kozoite-(La), and the transformation was completed
310 within 48 hours. Conversely, ANC transformed at 60 ºC directly to tengerite-(Nd)
311 within 14 hours with no lanthanite-(Nd) intermediate. After 48 hours only <5% of
312 tengerite-(Nd) transformed to kozoite-(Nd) [$NdCO_3(OH)$] (ICSD 6180). Not
313 surprisingly, with increasing temperatures at 95 ºC, the transformation was faster with
314 the lanthanite-(La) being almost fully transformed to kozoite-(La) after only 3 hours
315 (Fig. 6a, middle pattern; Table 1). However, it is worth noting that ANC remained
316 stable for at least 1 hour before crystallizing to tengerite-(Nd) and then transforming
317 completely to kozoite-(Nd) within 24 hours (middle pattern in Fig. 6b; Table 2).

318   When the amorphous precursors were reacted *hydrothermally* at temperatures
319 above 95 ºC, only anhydrous crystalline compounds were observed in both systems
320 (Table 2). At 165 ºC, kozoite-(Nd) was the main phase formed within the first 24
321 hours and with time its crystallization to a different polymorph, hydroxylbastnasite-

322   (Nd) [$NdCO_3(OH)$] (ICSD 2880), was observed. The isomorph, hydroxylbastnasite-

323   (La) [$LaCO_3(OH)$],[35,49] was the product of the transformation of kozoite-(La)

324   [$LaCO_3(OH)$] in the La system (Table 1). The phase evolution of the experiments

325   carried out at 220 ºC is similar to those at 165 ºC in that at both temperatures, the final

326   product was a hydroxylbastnasite-(REE) (Fig 6a and 6b, upper patterns). In the La

327   system, kozoite-(La) was always observed at the beginning of the experiment and its

328   transformation to hydroxylbastnasite-(La) [$LaCO_3(OH)$] was completed within 7

329   days. This evolution was similar in the Nd system, but in some cases kozoite-(Nd)

330   was not observed and hydroxylbastnasite-(Nd) formed directly from ANC within the

331   first three hours of reaction.

332   The comparison between the XRD patterns of REE-bearing carbonate

333   isomorphs obtained in identical experiments in the La and Nd systems showed larger

334   unit cell parameters and Scherrer crystallite sizes for the La-bearing carbonates

335   (lanthanite, kozoite, hydroxylbastnasite) than for the Nd-bearing isomorphs (Table 3).

336   The FEG-SEM images (Fig. 7 and 8) produced in the *wet-ambient* (21 ºC)

337   experiments showed that the first crystalline La-carbonate phase formed from the

338   ALC, lanthanite-(La), consisted of small (2-4 μm) crystal plates in rosette-like

339   aggregates with a maximum diameter of ~ 10 μm (Fig. 7a). After a long reaction time

340   (60 days), these transformed into 1-2 μm sized kozoite-La prisms (Fig. 7b). In the

341   *hydrothermal* experiments at 60 and 95 ºC, small oval particles (< 3 μm in size) were

342   observed (Fig. 7 c), corresponding to the neoformed crystals of kozoite-(La) identified

343   by XRD at 24 h (60 ºC) and 1 h (95 ºC). After further aging or above 165 ºC, kozoite-

344   (La) was present as well-developed elongated sub-micron-sized prisms grouped in

345   dumbbell shaped aggregates (up to 8 μm in size; Fig. 7d). Finally, these elongated

346   prisms transformed to triangular pyramids of hydroxylbastnasite-(La) (< 3 μm in size,

347   Fig. 7e), which were the crystalline end products at 165 and 220 ºC (Fig. 7f).

348   The morphologies observed in the Nd system (Fig. 8) at 21 ºC and after 4

349   hours were individual, non-aggregated crystal plates of lanthanite-(Nd) (up to 12 μm

350   in size, Fig. 8a) that transformed within 2 months to acicular tengerite-(Nd) crystals

351   with a maximum length of 3 μm (Fig. 8b). At 95 °C these tengerite-(Nd) crystals

352   clustered into sheets with dumbbell shapes (Fig. 8c). After several hours these in turn

353   transformed to kozoite-(Nd) (Fig. 8d), whose morphology was similar to that

354   described above for kozoite-(La). Kozoite-(Nd) was also observed at 165 °C and at

355   220 °C, forming directly from ANC (Fig SI-4). Finally, the morphology of

356   hydroxylbastnasite-(Nd) formed from kozoite-(Nd) at 165 and 220 °C was similar to

357   its La counterpart (Fig. 8e). However, in some experiments at 220 ºC

358   hydroxylbastnasite-(Nd) formed directly from ANC and lead to the formation of 10-

359   20 μm cauliflower-like structures composed of micrometer-sized ellipsoidal crystals

360   (Fig. 8f).

361   The FTIR spectra of the crystalline phases are dominated by much sharper

362   carbonate vibrations compared with the respective amorphous precursors. (Fig. SI-2

363   and SI-3, Table SI-2). Furthermore, in both systems the OH vibrations of the

364   lanthanites are much bigger confirming the higher water content (8 water molecules

365   pfu) compared to 5 water molecules pfu in the amorphous precursor, consistent with

366   the TGA data (Fig. 4). There is also a clear decrease of the structural water content at

367   higher temperatures, again confirming the transition from highly hydrous crystalline

368   lanthanites to the hydroxylated La and Nd carbonate phases. Furthermore, multiple

369   band splittings were observed in the spectra of the crystalline carbonates. For

370   example, the ν_3 asym. CO_3 peak at 1409 cm^{-1} (band 16 in Fig SI-2a, SI-3a, and Table

371   SI-2) in both the La and Nd kozoite (La/NdCO$_3$OH) appear as a split peak in the La

372   and Nd- hydroxylbastnasite (La/NdCO$_3$OH) with two peaks at 1425 and 1392 (bands

373   21 and 22 in Fig. SI-2a and SI-3a; Table SI-2).
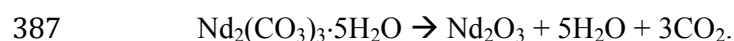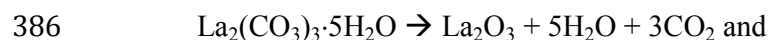
374

375   **4. DISCUSSION**

376

377   **4.1. Stability of amorphous La and Nd carbonates**

378

379   The crystallization of La and Nd carbonates takes place via poorly-ordered

380   hydrated metastable precursors. Taking into account the La:O or Nd:O ratios of 2:8

381   from the EDX analyses (Fig. 2), the presence of water and carbonate confirmed by

382   FTIR (Fig. 3) and the weight loss shown by thermogravimetric analyses (Fig. 4), we

383   deduced an idealized chemical formula for ALC and ANC as La$_2$(CO$_3$)$_3$·5H$_2$O and

384   Nd$_2$(CO$_3$)$_3$·5H$_2$O respectively. The decomposition reactions upon *dry-heating*

385   proceeded via the reactions:

386   La$_2$(CO$_3$)$_3$·5H$_2$O → La$_2$O$_3$ + 5H$_2$O + 3CO$_2$ and

387   Nd$_2$(CO$_3$)$_3$·5H$_2$O → Nd$_2$O$_3$ + 5H$_2$O + 3CO$_2$.

388   Our UV-Vis results (Fig. 5) revealed that the lifetimes of ALC and ANC were

389   ~ 9 and ~ 900 min respectively; ~ 1 and ~ 2 orders of magnitude longer than those

390   measured for the pure amorphous calcium carbonate (ACC), which is stable for <2

391   minutes at 21 °C.[5,13] Finally, our *hydrothermal* data (Tables 1 and 2) show that ANC

392   was stable for at least 1 hour even when reacted at 95 °C. Interestingly, two other

393   amorphous REE carbonates are known to be even more stable than ANC. These are

394   amorphous Dy carbonate (~3 days[36]) and amorphous Yb carbonate (AYbC), which

395   does not crystallize after one week of reaction at 120 °C. [32] Taken together, all these

396   data show that there is a direct proportionality between the ionic potential of the

397   REE^{3+} (2.60 Å^{-1} for La^{3+}, 2.78 Å^{-1} for Nd^{3+}, 3.03 Å^{-1} for Dy^{3+} and 3.22 Å^{-1} for Yb^{3+})

398   and the lifetimes of the REE carbonate precursors (9 min for ALC, 900 min for ANC,

399   2880 min for ADC and more than 10000 min for AYbC). Figure 9 shows this

400   proportionality: the larger the ionic potential of the REE^{3+}, the longer the stability of

401   the amorphous REE carbonate. A similar trend is known to occur with amorphous Ca

402   and Mg carbonates: amorphous Mg carbonate is stable for several days at ambient

403   temperature (ionic potential of Mg^{2+} = 3.07 Å^{-1},[50]) compared to ACC (<2 min; ionic

404   potential of Ca^{2+} = 2.02 Å^{-1},[5]). The breakdown of ACC prior to its crystallization is

405   known to occur by the progressive loss of structural water within the disordered

406   framework of the precursor.[11,12,50-52] Di Tommaso and de Leeuw (2010)[53] have

407   attributed the larger stability of amorphous Mg carbonate compared to ACC to the

408   stronger hydration shell of the Mg^{2+} ion: because of its larger ionic potential, the

409   energy needed to dehydrate the Mg^{2+} ion is larger than Ca^{2+}. In the case of amorphous

410   REE-bearing carbonates, the ionic potential of La^{3+} (2.60 Å^{-1}) is smaller than Nd^{3+}

411   (2.78 Å^{-1}), Dy^{3+} (3.03 Å^{-1}) or Yb^{3+} (3.19 Å^{-1}) and therefore the energy required to

412   dehydrate the La^{3+} ion in ALC will be lower compared to the Nd^{3+} ion in ANC.

413   Similarly, the exceptional stabilities of amorphous Dy carbonate[36] and amorphous Yb

414   carbonate[32] are in agreement with the larger ionic potential of these heavier

415   lanthanides.

416   The different crystallization pathways of ALC and ANC during the

417   thermodiffraction experiments (*dry heated*) (Fig. 1) suggest a higher dehydration

418   energy is needed for the Nd^{3+} ion in ANC compared to La^{3+} in ALC.

419   Thermodiffraction data (Fig. 1) showed that both ALC and ANC crystallized to

420    $REE_2O_2CO_3$ and then transformed to hexagonal REE_2O_3 above 400-450 °C, that is

421   after the decomposition of the CO_3 ion.[54] However, the transformation of cubic Nd-

422   dioxicarbonate to hexagonal Nd-oxide occurred via a cubic Nd-oxide (Fig. 1b, pattern

423   at 700 ºC). Fedorov et al. (2002)[55] observed that this transformation from cubic to

424   hexagonal Nd-oxide was completed at ~ 760 ºC and was irreversible. They explained

425   that this may be a consequence of crystallographic shear triggered by the release of

426   strongly bonded residual water. Conversely, in our La-system, hexagonal La-

427   dioxycarbonate transformed directly to hexagonal La-oxide above 700 °C because the

428   La^{3+} ion requires less energy than Nd^{3+} to dehydrate and thus all structural water had

429   been already released prior to reaching 700 °C; the sample weight remained constant

430   above 700 ºC in the La system (Fig. 4a). In the Nd system a small but progressive

431   mass loss is still observed above 700 ºC (Fig. 4b), which is consistent with the release

432   of structural water during the transformation from cubic to hexagonal Nd-oxide.

433

434   **4.2. The crystallization of La and Nd carbonates in solution: morphologies,**

435   **mechanisms and pathways.**

436

437   The breakdown of ALC and ANC in solution was translated into the

438   crystallization of a variety of La and Nd hydrated carbonates and hydroxycarbonates

439   with different compositions, structures and stabilities (Table 2S and 3S). Our

440   *hydrothermal* experiments revealed an evolution consistent with a progressive

441   dehydration, from the octahydrate lanthanite-(REE) $[REE_2(CO_3)_3·8H_2O]$ to the di-

442   trihydrate tengerite-(REE) $[REE_2(CO_3)_3·2-3H_2O]$, to kozoite-(REE) $[REECO_3OH]$

443   and finally to hydroxylbastnasite-(REE) $[REECO_3OH]$. This evolution is not

444   unexpected, as the anhydrous phases are usually more insoluble, denser and more

445   stable than the hydrated polymorphs. There are also some mineralogical differences

446   between both systems: in the La system, tengerite was completely absent because the

447   structure of lanthanite-type carbonates only forms when the ionic radii of the REE is

448   equal or larger than Nd, and tengerite-type carbonate structures are more typical for

449   heavier REE with ionic radii smaller than Nd.[32,49,56] Our data also show that the unit

450   cell parameters are larger in the La-bearing compounds compared to the Nd

451   counterparts (Table 3), again a consequence of the larger ionic radius of La than

452   Nd.[33,35]

453   The morphologies of the transformed crystalline La and Nd carbonates (Figs.

454   7 and 8) were only in some cases (Fig. 8c) similar to those reported in the literature.[42]

455   In many experiments the resulting morphologies were consistent with 'Category 2'

456   spherulites described by Gránásy et al. (2005)[57] and Andreassen et al. (2010).[58] The

457   best examples are kozoite-(La) (Fig. 7 c, d, e) and kozoite-(Nd) (Fig. 8 e), but also

458   tengerite-(Nd) (Fig. 8 c) and hydroxylbastnasite-(Nd) (Fig 8 f), the latter being very

459   similar to spherulitic vaterite morphologies (CaCO$_3$).[8,59] It is worth noting however

460   that in the La and Nd systems, these spherulitic morphologies were only found at

461   temperatures > 60 °C (La system) and > 95 °C (Nd system) and only when the

462   crystallization occured directly from the amorphous precursors. The only exception

463   was the crystallization of spherulitic kozoite > 60 °C as this formed either directly

464   from the amorphous precursor or through hydrated lanthanites (Table 1 and 2). A

465   summary of the crystallization products for the La and Nd carbonate systems at

466   different temperatures is shown in Fig. 10.

467   The spherulitic growth mechanism[57,60] results in the crystallization of

468   aggregates of particles with very distinctive spheroidal morphologies. It is considered

469   to occur via 'secondary' nucleation: after the formation of a single nucleus, the

470   growth takes place as a consequence of the continuous nucleation of new particles

471   with random orientations on the surfaces of the growing spherulite.[57] This 'secondary'

472   nucleation is usually referred to as 'growth front nucleation' and often leads to the

473   formation of sheaf-like morphologies.[57] In the carbonate system, spherulitic growth

474   has been described for the crystallization of vaterite,[8,58,61] calcite[62] and aragonite.[59]

475   This mechanism requires a strong crystallization driving force in order to maintain a

476   continuous growth front nucleation during spherulitic growth. In aqueous systems this

477   driving force is provided by a high level of supersaturation with respect to the solid

478   phase.

479   For carbonates, Andreassen et al (2010)[58] and Beck and Andreassen (2010)[62]

480   suggested that a saturation index greater than 2-3 is necessary for spherulitic growth

481   to occur. To determine the saturation index (SI) the activities of the ions in the

482   aqueous solution and the solubility product of the crystallizing solid phases need to be

483   known. Solubility data for La and Nd carbonates are limited to lanthanite-(La) and

484   lanthanite-(Nd).[46] Using these as analogues for all crystalline La and Nd carbonates

485   we calculated the SI values of lanthanite-(La) and lanthanite-(Nd) prior to solution

486   mixing (i.e. before the formation of any amorphous precursor) as 12.91 and 11.01.

487   These are larger than the critical values suggested by Andreassen et al (2010)[58] and

488   Beck and Andreassen (2010)[62] thus, it is not surprising that we observed spherulitic

489 growth. The high Si values suggest that the supersaturation condition for spherulitic

490 growth would have been fulfilled if the crystals were formed directly from solution.

491 Nevertheless in our experiments La- and Nd-bearing crystalline carbonates formed via

492 amorphous precursors, meaning that the aqueous solution had to be in equilibrium

493 with ALC or ANC prior to the formation of the crystalline phases. There is however,

494 no data about the solubility products of these precursors available and therefore

495 calculating SI values for crystalline La and Nd carbonates when the aqueous solution

496 was in equilibrium with ALC or ANC is impossible. Yet, it is well known that

497 amorphous precursors are usually more soluble than the crystalline phases they

498 transform into. The best-known example is ACC, which is one order or magnitude

499 more soluble than vaterite or calcite.[48]

500 Furthermore, as discussed above, the breakdown of amorphous precursors

501 involves temperature-dependent dissolution and dehydration processes.[5,11-13,50-52] This

502 means that the faster an amorphous precursor breaks down, the bigger the

503 supersaturation levels are during the crystallization, favouring spherulitic growth. In

504 the La and Nd system, the spherulitic morphologies provide unambiguous evidence of

505 large supersaturation levels during crystallization. Therefore by taking all these data

506 as a whole, we hypothesize that > 60 °C, high supersaturation levels were reached and

507 this promoted the rapid breakdown of the La and Nd amorphous carbonate precursors,

508 leading to the crystallization of La and Nd carbonates via a spherulitic growth process

509 (e.g., Fig SI-4).

510 In addition to supersaturation, two other factors need to be taken into account

511 in order to understand the drive to grow spherulitic morphologies in the La and Nd

512 systems: a) ionic potentials and b) heating process. We have discussed above that the

513 dehydration energies needed for the breakdown of ALC and ANC differ and that this

514 is a consequence of the difference in ionic potentials between the La^{3+} and the Nd^{3+}

515 ions. This was evidenced in both the *dry-heated* (Fig. 2) and UV-Vis (*wet-ambient*)

516 (Fig. 5) experiments. Note however, that if the desired thermal regime in the reactor is

517 reached slowly due to thermal buffering effects, the amorphous precursor may break

518 down before the target *hydrothermal* temperature is reached. This may lead to a

519 slower dissolution of the amorphous precursor and hence a slower achievement of the

520 high supersaturation levels needed for the next stage. Therefore, the combination of

521 high supersaturation levels, differences in ionic potentials and lifetime of the

522   precursor phase (also dependent on ionic potential of the REE^{3+} ion) all affect the

523   crystallization of La and Nd carbonates.

524

525   Spherulitic growth occurred at 95 °C in the Nd system and 60 °C in the La

526   system because the Nd^{3+} ion in ANC required a higher dehydration energy compared

527   to the La^{3+} ion in ALC. This also explains the fact that at temperatures above 95 °C it

528   was possible to obtain spherulitic tengerite-(Nd) (at 95 °C), kozoite-(Nd) (at 165 °C)

529   and hydroxylbastnasite-(Nd) (at 220 °C) directly from the precursor. However, when

530   these minerals were obtained as a product of recrystallization from a different

531   crystalline Nd carbonate (e.g.: hydroxylbastasite from kozoite, Fig. 8e), the

532   morphologies were not spherulitic. We suggest that in these cases the difference in

533   solubility of the minerals was too small to promote spherulitic growth, similar to what

534   happens in the $CaCO_3$ system (e.g. vaterite-calcite transformation[5,13]).

535

536   In the La system, once lanthanite-(La) formed, it recrystallized to kozoite-

537   (La), a transformation that also involves a dehydration process. At ambient

538   temperature, this recrystallization was too slow to promote spherulitic growth, but

539   lanthanite rapidly transformed to spherulitic kozoite-(La) at higher (60 °C)

540   temperatures. It is possible to explain this spherulitic growth of kozoite-(La) from

541   lanthanite-(La) at greater than 60 °C because of the highly hydrated and layered

542   structure of lanthanite[49] and the lower dehydration energy of La^{3+} compared to Nd^{3+},

543   which would allow a rapid dissolution of lanthanite at these temperatures (similarly,

544   in the Nd system the dissolution of tengerite-(Nd) also seems to be fast enough to

545   promote the spherulitic growth of kozoite-(Nd)). At 165 and 220 °C no lanthanite-

546   (La) was observed and kozoite-(La) most probably formed directly from ALC.

547   However, due to the short lifetime of ALC, the formation of spherulitic

548   hydroxylbastnasite-(La) at 220 °C did not occur in our experiments because the

549   primary crystallization of spherulitic kozoite-(La) took place before the final

550   experimental temperature was reached. Once kozoite-(La) crystallized, its

551   transformation to hydroxylbastnasite-(La) via spherulitic growth was not favoured

552   because the small differences in solubility between kozoite-(La) and

553   hydroxylbastnasite-(La). Our experiments suggest that the kozoite-hydroxylbastnasite

554   transformation is likely to occur via a dissolution-reprecipitation mechanism (SEM

555   images and XRD data, Fig. 7e and Table 1).

556

557   The stronger hydration shell of the Nd^{3+} ion compared to the La^{3+} also affects

558 the Scherrer crystallite size in the hydrothermal experiments. The Scherrer crystallite

559 sizes were always smaller in the Nd-bearing polymorphs than in their La-bearing

560 isomorphs (Table 3). Similarly to the dry-heated experiments, we consider that this

561 effect is produced by the higher energy needed for release of water molecules from

562 the Nd^{3+} ion compared to La^{3+} before incorporation to the lattice of the growing

563 crystals. A similar effect has also been observed for the Mg^{2+} ion in the $CaCO_3$

564 carbonate system.[63] In the Nd system, the release of water from the hydration shell of

565 Nd^{3+} would be incomplete,[55] especially at low temperatures, affecting the crystallinity

566 of the forming solid.

567

568

569 **5. CONCLUSIONS**

570

571   The crystallization of La or Nd bearing-carbonates is always initiated by the

572 nucleation and growth of amorphous La or Nd carbonate precursors. Both of the

573 precursors are highly hydrated nanoparticulate compounds with similar spherical

574 morphologies and sizes. However, the most striking difference between the

575 amorphous La and Nd precursors is related to the stabilities. These depend directly on

576 the ionic potential of the REEs: the higher ionic potential the longer the lifetime of the

577 amorphous phase because the energy needed to dehydrate the Nd^{3+} ion is higher

578 compared to the La^{3+}. This is translated into a two order of magnitude longer lifetime

579 of ANC than ALC. After the breakdown of the precursors under different *dry heated*,

580 *ambient* or *hydrothermal* conditions and over a range of temperatures, they transform

581 to a variety of crystalline REE carbonates with different structures, compositions and

582 stabilities. Hydrated carbonates like lanthanite-(REE) and tengerite (only stable for

583 the Nd system) were obtained at lower temperatures (21, 60 and 95 ºC), whereas at

584 higher temperatures (165 and 220 ºC) anhydrous carbonates like kozoite-(REE) and

585 hydroxylbastnasite-(REE) were dominant. The morphology of these minerals depends

586 on the temperature and the kinetics of the crystallization. The general behaviour is

587 that above 60 ºC (La system) and 95 °C (Nd system) the minerals develop spherulitic

588 morphologies when they crystallize directly form amorphous precursors. This

589 development of the spherulitic growth requires high supersaturation levels that can

590 only be obtained by the rapid dissolution of the amorphous precursors or the hydrated

591 crystalline carbonates in some specific cases.

592 　　　The amorphous La and Nd carbonates have an enormous potential in the

593 material science industry if they can be exploited for the controlled development of

594 REE-bearing crystalline carbonates with specific properties and morphologies. Our

595 results show transformation products of varying morphologies resulting from different

596 crystallization mechanisms that operate even with a simple transformation method,

597 opening new perspectives on the synthesis of REE-bearing carbonates for advanced

598 technological applications. This study describes for the first time the crystallization

599 sequences of these REE-bearing carbonates. This knowledge will be essential in the

600 design of new separation methods of La and Nd during processing of REE ores.

601

602

603 **6. ACKNOWLEDGEMENTS**

604

612

613 **7. REFERENCES**

614 　　1　F. C. Meldrum, H. Cölfen, *Chem. Rev.* 2008, **108**, 4332.

615 　　2　F. C. Meldrum, R. P. Sear, *Science* 2008, **322**,1802-1803.

616 　　3　L. B. Gower, *Chem. Rev.* 2008, **108**, 4551.

617 　　4　J. D. Rodriguez-Blanco, S. Shaw, L. G. Benning, *Mineral. Mag.* 2008, **72**,

618 　　　　283.

619 　　5　J. D. Rodriguez-Blanco, S. Shaw, L. G. Benning, *Nanoscale*, 2011, **3**, 265.

620 　　6　T. Roncal-Herrero, J. D. Rodriguez-Blanco, L. G. Benning, E. H. Oelkers,

621 　　　　*Cryst. Growth Des.* 2009, **9**, 5197.

622 　　7　D. J. Tobler, S. Shaw, L. G. Benning, *Geochim. Cosmochim. Ac.* 2009, **73**,

623 　　　　5377.

624   8   P. Bots, J. D. Rodriguez-Blanco, T. Roncal-Herrero, S. Shaw, L. G. Benning,
625   *Cryst. Growth Des.* 2012, **12**, 3806.

626   9   A. E. S. Van Driessche, L. G. Benning, J. D. Rodriguez-Blanco, M. Ossorio,
627   P. Bots, J. M. García-Ruiz, *Science,* 2012, **336**, 69.

628   10 T. Roncal-Herrero, J. D. Rodriguez-Blanco, E. H. Oelkers, L. G. Benning, *J.
629   Nanopart. Res.* 2011, **13**, 4049.

630   11 A. V. Radha, T. Z. Forbes, C. E. Killian, P. U. P. A. Gilbert, A. Navrotsky, *P.
631   Natl. Acad. Sci. U.S.A.* 2010, **107**, 16348.

632   12 A. L. Goodwin, F. M. Michel, B. L. Phillips, D. A. Keen, M. T. Dove, R. J.
633   Reeder, *Chem. Mater.* 2010, **22**, 3197.

634   13 J. D. Rodriguez-Blanco, S. Shaw, L. G. Benning, *Am. Mineral.* 2015, In press.
635   doi: 10.2138/am.2014.4963

636   14 J. D. Rodriguez-Blanco, S. Shaw, P. Bots, T. Roncal-Herrero, L. G. Benning,
637   *Geochim. Cosmochim. Ac.* 2014, **127**, 204.

638   15 Z. Z. Zyman, D. V. Rokhmistrov, V.I. Glushko, *J. Mater. Sci.: Mater. Med.*
639   2010, **21**,123.

640   16 C. Combes, C. Rey, *Acta Biomater.* 2010, **6**, 3362.

641   17 D. Bauer, D. Diamond, J. Li, M. McKittrick, D. Sandalow, P. Telleen Critical
642   Materials Strategy. US Department of Energy. Washington, DC, 2011.
643   http://energy.gov/node/349057

644   18 G. P. Hatch, *Elements*, 2012, **8**, 341.

645   19 A. R. Chakhmouradian, F. Wall, *Elements*, 2012, **8**, 333.

646   20 S. B. Castor, J. B. Hedrick, in Industrial Minerals and Rocks. (Eds. J. E.
647   Kogel, N. D. Trivedi, J. M. Barker). Society for Mining, Metallugy and
648   Exploration, 2006, pp. 769-792

649   21 Y. C. Cui, J.H. Liu, X. W. Ren, X. F. Shi, *J. Rare Earth.* 2009, **27**, 169.

650   22 A. J. Ragavan, D. V. Adams, J. Nucl. Mater. 2009, **389**, 394.

651   23 A. P. Gysi, A. E. William-Jones, *Chem. Geol.* 2015, **392**, 87.

652   24 L. B. Railsback, *Geology*, 2003, **31**, 737.

653   25 G. H. Cartledge, *Journal of the American Chemical Society*, 1928a, **50**, 2855.

654   26 G. H. Cartledge, *Journal of the American Chemical Society*, 1928b, **50**, 2863.

655   27 H. Gamsjäger, *Pure Appl. Chem.* 1995, **67**, 535.

656   28 H. Niu, Q. Min, Z. Tao, J. Song, C. Mao, S. Zhang, Q. Chen, *J. Alloy. Compd.*
657   2011, **509**, 744.

658 29 B. Bakiz, F. Guinneton, M. Arab, A. Benlhachemi, J. R. Gavarria, *M. J.*
659   *Condensed Matter.* 2010, **12**, 60.

660 30 M. J. Norman, J. E. Andrew, T. H. Bett, R. K. Clifford, J. E. England, N.W.
661   Hopps, K. W. Parker, K. Porter, M. Stevenson, *Appl. Optics*, 2002, **41**, 3497.

662 31 K. V. Kumar, A. S. Kumar, *Opt. Mater.* 2012, **35**, 12.

663 32 K. Nagashima, H. Wakita, A. Mochizuki, *Bulletin of the Chemical Society of*
664   *Japan.* 1973, **46**, 152.

665 33 Z. Han, P. Xu, K. R. Ratinac, G. Q. Lu, *J. Cryst. Growth.* 2004, **273**, 248.

666 34 S. Liu, R. Ma, R. Jiang, F. Luo, *J. Cryst. Growth.* 1999, **206**, 88.

667 35 K. Michiba, T. Tahara, I. Nakai, R. Miyawaki, S. Matsubara, *Z. Kristallogr.*
668   2011, **226**, 518.

669 36 B. Vallina, J. D. Rodriguez-Blanco, A. P. Brown, J. A. Blanco, L. G. Benning,
670   *J. Nanopart. Res.* 2013, **15***, 1438.

671 37 J. M. Haschke, *J. Solid State Chem.* 1975, **12**, 115.

672 38 M. L. Panchula, M. Akinc, *Journal of the European Ceramic Society.* 1996,
673   **16**, 833.

674 39 J. W. Ding, Y. X. Li, H. Ting, X. M. Luo, Y. Yang, X. B. He, *Chinese J.*
675   *Inorg. Chem.* 2005, **21***, 1213.

676 40 Y. L. Wu, W. L. Sun, X. P. Feng, X. Xu, Y. X. Li, *Chinese J. Inorg. Chem.*
677   2007, **23**, 550.

678 41 S. Liu, R. Ma, R. Jiang, F. Luo, *J. Cryst. Growth*. 1999, **203**, 454.

679 42 Y. X. Li, T. Huang, J. M. Luo, X. Z. Zhou, *Chinese J. Inorg. Chem.* 2005, **21**,
680   1561.

681 43 A. L. Patterson, *Phys. Rev.* 1939, **56***, 978.

682 44 A. A. Coelho, TOPAS: General Profile and Structure Analysis Software for
683   Powder Diffraction Data, 2003.

684 45 D. Parkhurst, *Water Res. Invest. Report.* 1998**.** PHREEQC (Version 2)-A
685   Computer Program for Speciation, Batch-Reaction, One Dimensional
686   Transport, and Inverse Geochemical Calculations. USGS 99.

687 46 M. E. Essington, S. V. Mattigod, *Solid Sci. Soc. Am. J.* 1985, **49**, 1387.

688 47 P. Bayliss, A. A. Levinson, Am. Mineral. 1988, **73**, 422.

689 48 L. Brečević, A. E. Nielsen, *J. Cryst. Growth*. 1989, **98**, 504.

690   49 M. Leskelä, L. Niinistö, in Handbook of the Physics and Chemistry of Rare
691   Earths (Eds: K. A. Gschneidner, Jr. L. Eyring), Elsevier B.V., 1986, pp. 203-
692   334.

693   50 A. Navrotsky, *Mineral. Mag.* 2012, **76**, 2159.

694   51 M. Saharay, A. O. Yazaydin, R. J. Kirkpatrick, *J. Phys. Chem. B.* 2013, **117**,
695   3328.

696   52 P. Raiteri, J. D. Gale, *J. Am. Chem. Soc.* 2010, **132**, 17623.

697   53 D. Di Tommaso, N. H. de Leeuw, *Phys. Chem. Chem. Phys.* 2010, **12***,* 894.

698   54 A. K. Galwey, M. E. Brown, in Thermal decomposition of ionic solids.
699   Elsevier B.V. 1999, pp. 345-364.

700   55 P. P. Fedorov, M. V. Nazarkin, R. M. Zakalyukin, *Crystallogr. Rep.+.* 2002,
701   **47**, 281.

702   56 V. Philippini, T. Vercouter, A. Chaussé, P. Vitorge, *J. Solid State Chem.* 2008,
703   **181**, 2143.

704   57 L. Gránásy, T. Pusztai, G. Tegze, J. A. Warren, J. F. Douglas, *Phys. Review E.*
705   2005, **72**, 011605.

706   58 J. P. Andreassen, E. M. Flaten, R. Beck, A. E. Lewis, *Chem. Eng. Res. Des.*
707   2010, **88**, 1163.

708   59 K. K. Sand, J. D. Rodriguez-Blanco, E. Makovicky, L. G. Benning, S. S. L.
709   Stipp, *Cryst. Growth. Des.* 2012, **12 (2)**, 842.

710   60 A. G. Shtukenberg, Y. O. Punin, E. Gunn, B. Kahr, *Chem Rev*, 2012, **112**,
711   1805.

712   61 J. P. Andreassen, *J. Cryst. Growth.* 2005, **274**, 256.

713   62 R. Beck, J. Andreassen, *Cryst. Growth Des.* 2010, **10**, 2934.

714   63 A. Mucci, J. W. Morse, *Geochim. Cosmochim. Ac.* 1983, **47**, 217.

715

716

717

718   **FIGURE CAPTIONS:**

719

720   **Figure 1.-** Selected powder X-ray diffraction patterns recorded from the lanthanum
721   (a) and neodymium (b) solid precursor phases (bottom patterns in both cases) and

22

722   their crystallization products when *dry-heated* from 25 °C to 1000 °C. The asterisks

723   in the bottom patterns indicate the position of the humps in the amorphous precursors.

724

725   **Figure 2.-** TEM images of the pristine amorphous lanthanum (a) and neodymium (c)

726   carbonate precursor phases and the crystalline transformation products produced by

727   irradiation with the high energy electron beam of the TEM for a few seconds (b and d

728   respectively). The insets show respective EDX spectra with the Cu peaks coming

729   from the Cu support grid. Standardless quantification from these spectra gave a La:O

730   and Nd:O atomic ratio of 2:8.

731

732   **Figure 3.-** FTIR spectra of ALC and ANC showing the large OH band (1) and the

733   principal carbonate bands (2-6). Details of the band assignments are presented in

734   Table SI-1 and discussed in the text.

735

736   **Figure 4.-** TGA (sample weight loss and weight loss rate curves) of the poorly-

737   ordered precursor: ALC (a), ANC (b). The curves show a progressive loss of water

738   and the final carbonate decomposition between 450 and ~ 650 ºC.

739

740   **Figure 5.-** Turbidity curves from the i*n situ* and time resolved UV-VIS experiments,

741   showing the evolution of the crystallization of ALC and ANC in aqueous solution at

742   ambient temperature.

743

744   **Figure 6.-** Powder X-ray diffraction patterns of the solids obtained in the (a) La and

745   (b) Nd systems from *wet-ambient* conditions (21 °C) and at *hydrothermal* (60-220 ºC)

746   conditions. The patterns were indexed to: (a) $La_2(CO_3)_3 \cdot 8H_2O$, kozoite-(La)

747    $LaCO_3(OH)$ and hydroxylbastnasite-(La) $[LaCO_3(OH)]$ and (b) $Nd_2(CO_3)_3 \cdot 2\text{-}3H_2O$,

748    $Nd_2(CO_3)_3 \cdot 8H_2O$,   kozoite-(Nd) $[NdCO_3(OH)]$,   hydroxylbastnasite-(Nd)

749    $[NdCO_3(OH)]$. Full details about the indexing are presented in Fig SI-1.

750

751   **Figure 7**.- FEG-SEM images of the crystalline lanthanum end product phases of the

752   *wet-ambient* and *hydrothermal* treatments: (a) $La_2(CO_3)_3 \cdot 8H_2O$ rosettes obtained at 21

753   ºC. (b) Well-faceted prisms of kozoite-(La) obtained at 21 ºC. (c) $La_2(CO_3)_3 \cdot 8H_2O$

754   crystals and ellipsoidal crystals of kozoite-(La) at the beginning of the transformation

755   (d) Dumbbell-shaped kozoite-(La) obtained at 165 ºC. (e) Transformation of the

756   dumbbell-shaped kozoite-(La) into triangular hydroxylbastnasite-(La) pyramids (f)

757   Hydroxylbastnasite-(La) pyramids obtained as the final product of the *hydrothermal*

758   treatments at 165 ºC; the same final product with the same shapes were also obtained

759   at 220 °C.

760

761   **Figure 8**.- FEG-SEM images of the crystalline neodymium end product phases of the

762   *wet-ambient* and *hydrothermal* treatments: (a) crystal plates of $Nd_2(CO_3)_3 \cdot 8H_2O$

763   obtained at 21 ºC. (b) Acicular needle-like crystals of tengerite-(Nd) obtained at 60

764   ºC. (c) Spherulitic, plate-like tengerite-(Nd) obtained at 95 ºC (d) Dumbbell-shaped

765   kozoite-(Nd) obtained at 95 ºC. (e) Triangular hydroxylbastnasite-(Nd) pyramids

766   obtained at 165 °C. (f) Spherulitic hydroxylbastnasite-(Nd) [$Nd(CO_3)OH$] obtained as

767   a direct product of the transformation of the amorphous Nd carbonate precursor,

768   ANC, at 220 ºC.

769

770   **Figure 9**.- Plot showing the proportionality between the stability of the La, Nd, Dy

771   and Yb amorphous carbonate precursors and the ionic potential of the REE^{3+} involved

772   in the precursor.

773

774   **Figure 10**.- Summary of the crystallization products for the La and Nd systems at

775   different temperatures in the *wet-ambient* and *hydrothermal* treatments.

776

777   **Table 1**. Experimental conditions as well as identities and morphologies of the solid

778   lanthanum carbonate phases obtained from the *dry-heated*, *ambient and hydrothermal*

779   treatments.

780

781   **Table 2**. Experimental conditions as well as identities and morphologies of the solid

782   neodymium carbonate phases obtained from the *dry-ambient, dry-heated, wet-ambient*

783   *and hydrothermal* treatments.

784

785   **Table 3**.- Comparison of the cell parameters and crystallite sizes of La or Nd bearing

786   minerals. Unit cell parameters are listed as a function of ionic radius for lanthanite,

787   kozoite and hydroxylbastnasite and have been determined as a function of the ionic

788   radius of the trivalent rare earth ion species.

789

790

Table 1. Experimental conditions with identities and morphologies of the solid lanthanum carbonate phases obtained from the *dry-heated*, *wet-ambient and hydrothermal* treatments.

| Exp. conditions	Temp [°C]	Time [h]	Identity of the solid phase(s) (in order of abundance)	Morphology of the most abundant phase (TEM/SEM)
Dry-ambient	25	48	ALC, $La_2(CO_3)_3 \cdot 5H_2O)$, (x < 5), amorphous	Spheres
		> 48	Lanthanite-(La) $[La_2(CO_3)_3 \cdot 8H_2O]$ (100 %)	–
Dry-heated	25-1000	0 - 13 (1 °C/min ramp)	ALC, $La_2(CO_3)_3 \cdot 5H_2O$, (x < 5), amorphous ($\leq$ 400 °C)	Spheres
			Monoclinic La-dioxicarbonate, $La_2O_2CO_3$, a=4.080 Å, b=13.509 Å, c=4.072 Å (450-700 ºC)	(Not imaged)
			Hexagonal La-dioxicarbonate, $La_2O_2CO_3$, a=b=4.078 Å, c=15.950 Å (~ 700-800 °C)	(Not imaged)
			La-oxide, La_2O_3 ($\geq$800 °C)	(Not imaged)
Wet-ambient	21	4	Lanthanite-(La) $[La_2(CO_3)_3 \cdot 8H_2O]$ (100 %)	Rosettes
		24	Lanthanite-(La) $[La_2(CO_3)_3 \cdot 8H_2O]$ (100 %)	Rosettes
		1440	Kozoite-(La) $[LaCO_3(OH)]$ (100 %)	Rhombohedral prisms
Hydrothermal	60	4	Lanthanite-(La) $[La_2(CO_3)_3 \cdot 8H_2O]$ (100 %)	Rosettes
		14	Lanthanite-(La) $[La_2(CO_3)_3 \cdot 8H_2O]$(100 %)	Rosettes
		24	Lanthanite-(La) $[La_2(CO_3)_3 \cdot 8H_2O]$ (~ 60%); Kozoite-(La) $[LaCO_3(OH)]$ (~ 40%)	Rosettes Ovoidal particles
		48	Kozoite-(La) $[LaCO_3(OH)]$ (100 %)	Dumbbell shapes
	95	1	Lanthanite-(La) $[La_2(CO_3)_3 \cdot 8H_2O]$ (~ 83%); Kozoite-(La) $[LaCO_3(OH)]$ (~ 17%)	Rosettes; Oval particles
		3	Kozoite-(La) $[LaCO_3(OH)]$ (~ 99%); Lanthanite-(La) $[La_2(CO_3)_3 \cdot 8H_2O]$ (~ 1 %)	Dumbbell shapes Rosettes
		24	Kozoite-(La) $[LaCO_3(OH)]$ (100 %)	Dumbbell shapes
	165	4	Kozoite-(La) $[LaCO_3(OH)]$ (~ 88%); Hydroxylbastnasite-(La) $[LaCO_3(OH)]$ (~ 12%)	Dumbbell shapes; Triangular pyramids
		24	Kozoite-(La) $[LaCO_3(OH)]$ (~ 70%); Hydroxylbastnasite-(La) $[LaCO_3(OH)]$ (~ 30%)	Dumbbell shapes; Triangular pyramids
	220	4	Kozoite-(La) $[LaCO_3(OH)]$ (~ 32 %); Hydroxylbastnasite-(La) $LaCO_3(OH)$ (~ 68 %)	Dumbbell shapes; Triangular pyramids
		24	Hydroxylbastnasite-(La) $LaCO_3(OH)$ (~ 76 %); Kozoite-(La) $[LaCO_3(OH)]$ (~ 24 %)	Triangular pyramids; Dumbbell-like shapes
		168	Hydroxylbastnasite-(La) $LaCO_3(OH)$ (100 %)	Triangular pyramids

Table 2. Experimental conditions with identities and morphologies of the solid neodymium carbonate phases obtained from the *dry-ambient*, *dry-heated*, *wet-ambient and hydrothermal* treatments. The symbol (*) denotes that in some of the experiments run at 220 °C kozoite-(Nd) was not identified after 4 and 24 hours and hydroxylbastnasite-(Nd) was the only solid phase found

Exp. conditions	Temp [°C]	Time [h]	Identity of the solid phase(s) (in order of abundance)	Morphology of the most abundant phase (TEM/SEM)
Dry-ambient	**25**	4320 (6 months)	ANC, $Nd_2(CO_3)_3 \cdot xH_2O$ (x < 5), amorphous	Spheres
Dry-heated	25-1000	0 - 13 (1 °C/min ramp)	ANC, $Nd_2(CO_3)_3 \cdot xH_2O$ (x < 5), amorphous (≤ 450 °C)	Spheres
			Hexagonal Nd-dioxicarbonate $Nd_2O_2CO_3$ (a=b=3.988 Å, c=13.120 Å) (~ 550 °C)	(Not imaged)
			Cubic Nd-oxide Nd_2O_3 (a=b=c=11.072 Å) (~ 700 °C)	(Not imaged)
			Hexagonal Nd-oxide Nd_2O_3 (a=b=3.830 Å, c=5.999 Å) (≥ 800 °C)	(Not imaged)
Wet-ambient	21	4	ANC, $Nd_2(CO_3)_3 \cdot xH_2O$ (x < 5), amorphous	Spheres
		24	Lanthanite-(Nd) $[Nd_2(CO_3)_3 \cdot 8H_2O]$	crystal plates
		1440	Tengerite-(Nd) $[Nd_2(CO_3)_3 \cdot 2.5H_2O)]$ (~ 93%); Lanthanite-(Nd) $[Nd_2(CO_3)_3 \cdot 8H_2O]$ (~ 7%)	Acicular crystals crystal plates
Hydrothermal	60	4	ANC, $Nd_2(CO_3)_3 \cdot xH_2O$ (x < 5), amorphous	Spheres
		14	Tengerite-(Nd) $[Nd_2(CO_3)_3 \cdot 2.5H_2O)]$ (100%)	Acicular crystals
		24	Tengerite-(Nd) $[Nd_2(CO_3)_3 \cdot 2.5H_2O)]$ (100%)	Acicular crystals
		48	Tengerite-(Nd) $[Nd_2(CO_3)_3 \cdot 2.5H_2O)]$ (~ 95%); Kozoite-(Nd) $[NdCO_3(OH)]$ (~ 4%)	Acicular crystals Oval particles
	95	1	ANC, $Nd_2(CO_3)_3 \cdot xH_2O$ (x < 5), amorphous	Spheres
		3	Tengerite-(Nd) $[Nd_2(CO_3)_3 \cdot 2.5H_2O)]$ (~ 60%) Kozoite-(Nd) $[NdCO_3(OH)]$ (~ 40%)	crystal plates (spherulitic) Dumbbells (spherulitic)
		24	Kozoite-(Nd) $[NdCO_3(OH)]$ (100%)	Dumbbells (spherulitic)
	165	4	Kozoite-(Nd) $[NdCO_3(OH)]$ (~ 88%); Hydroxylbastnasite-(Nd) $[NdCO_3(OH)]$ (~ 12%)	Elongated prisms; Triangular Pyramids

		24	Kozoite-(Nd) [NdCO$_3$(OH)] (~ 65%); Hydroxylbastnasite-(Nd) [NdCO$_3$(OH)](~ 35%)	Elongated prisms; Triangular pyramids
		4	Kozoite-(Nd) [NdCO$_3$(OH)] (~ 41%); (*) Hydroxylbastnasite-(Nd) [NdCO$_3$(OH)] (~ 59%)	Elongated prisms; Triangular pyramids
	220	24	Hydroxylbastnasite-(Nd) [NdCO$_3$(OH) (~ 99%); Kozoite-(Nd) [NdCO$_3$(OH)] (~ 1%) (*)	Triangular pyramids Elongated prims
		168	Hydroxylbastnasite-(Nd) [NdCO$_3$(OH)] (100%)	Triangular pyramids

.

Table 3. Comparison of the cell parameters and crystallite sizes of La or Nd bearing minerals. Unit cell parameters as a function of ionic radius for lanthanite, kozoite and hydroxylbastnasite have been determined as a function of the ionic radius of the trivalent rare earth ion species.

Mineral	Cell parameters	La	Nd	Unit cell parameters as a function of ionic radius of the RE^{3+} ion	Crystallite size La [nm]	Crystallite size Nd [nm]
Lanthanite (21 ºC)	a [Å]	8.9894	8.8889	a = 1.4357 r + 7.3383	> 200	31
	b [Å]	9.5734	9.4299	b = 2.05 r + 7.2159		
	c [Å]	17.0265	16.8996	c = 1.8129 r + 14.942		
	Vol [Å³]	1465	1416	–		
Tengerite (60 ºC)	a [Å]	-	6.2288	–	–	14
	b [Å]	-	9.4316	–		
	c [Å]	-	15.5623	–		
	Vol [Å³]	-	914	–		
Kozoite (165 ºC)	a [Å]	5.0357	4.9662	a = 0.9929 r + 3.8939	113	54
	b [Å]	8.5835	8.4982	b = 1.2186 r + 7.1821		
	c [Å]	7.4023	7.2325	c = 2.4257 r + 4.6127		
	Vol [Å³]	320	305	–		
Hydroxylbastnasite (220 ºC)	a [Å]	12.6294(95)	12.3579	a = 3.8786 r + 8.169	121	109
	c [Å]	10.0321(78)	9.9025	c = 1.8514 r + 7.903		
	Vol [Å³]	1386	1309	–		
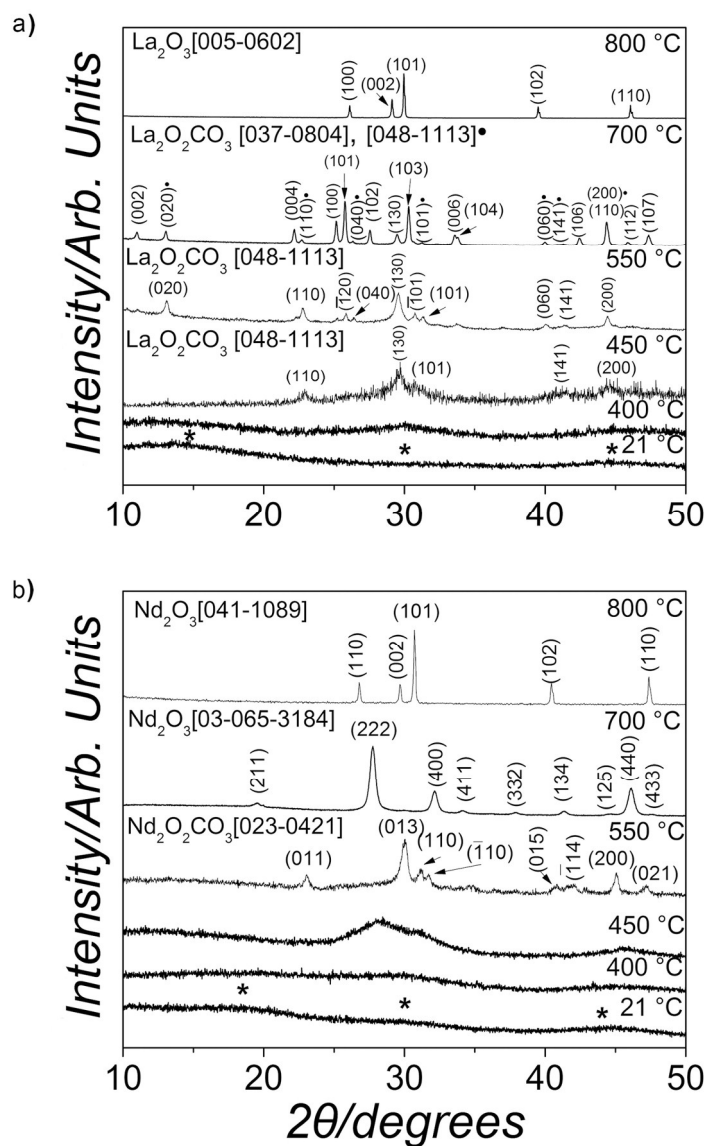
Selected powder X-ray diffraction patterns recorded from the lanthanum (a) and neodymium (b) solid precursor phases (bottom patterns in both cases) and their crystallization products when dry-heated from 25 °C to 1000 °C. The asterisks in the bottom patterns indicate the position of the humps in the amorphous precursors.
130x205mm (300 x 300 DPI)
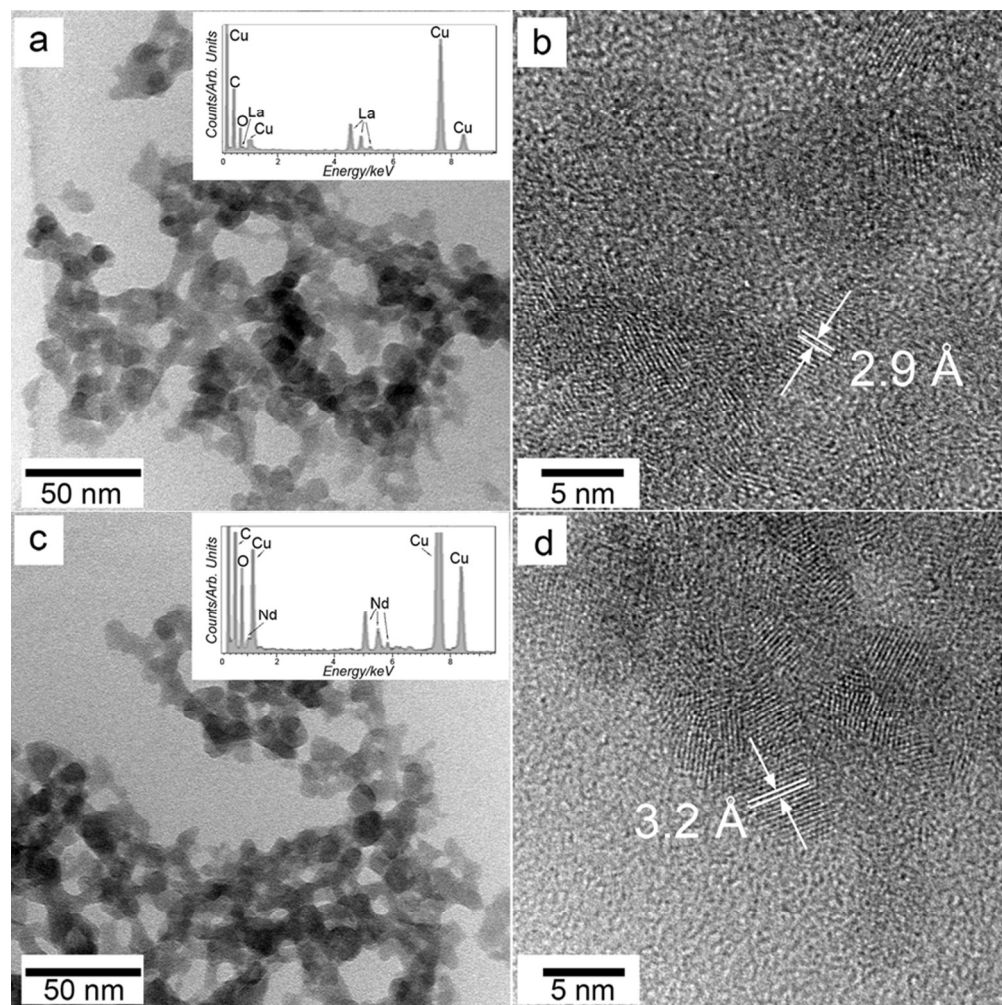
TEM images of the pristine amorphous lanthanum (a) and neodymium (c) carbonate precursor phases and the crystalline transformation products produced by irradiation with the high energy electron beam of the TEM for a few seconds (b and d respectively). The insets show respective EDX spectra with the Cu peaks coming from the Cu support grid. Standardless quantification from these spectra gave a La:O and Nd:O atomic ratio of 2:8.
82x82mm (300 x 300 DPI)
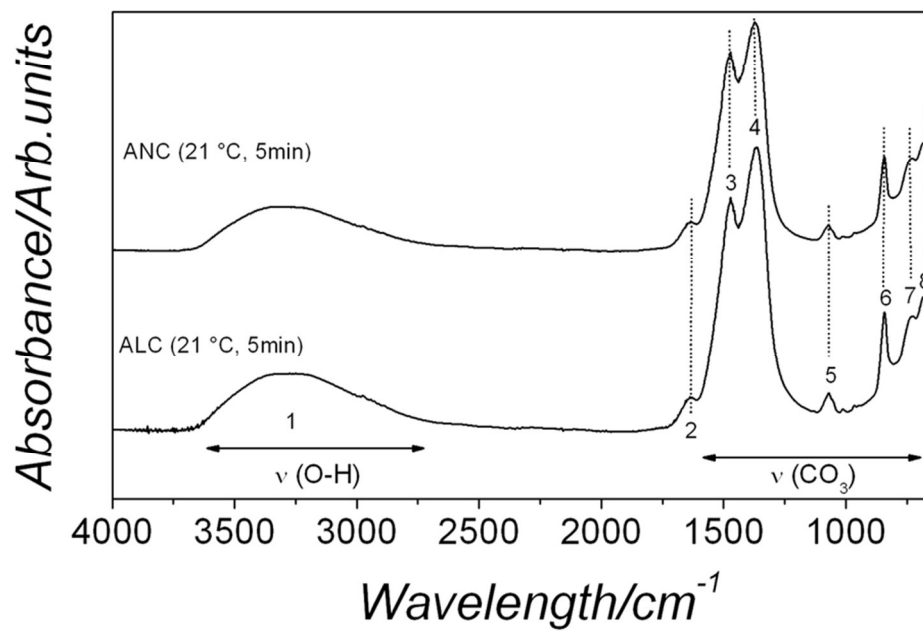
FTIR spectra of ALC and ANC showing the large OH band (1) and the principal carbonate bands (2-6).
Details of the band assignments are presented in Table SI-1 and discussed in the text.
82x56mm (300 x 300 DPI)
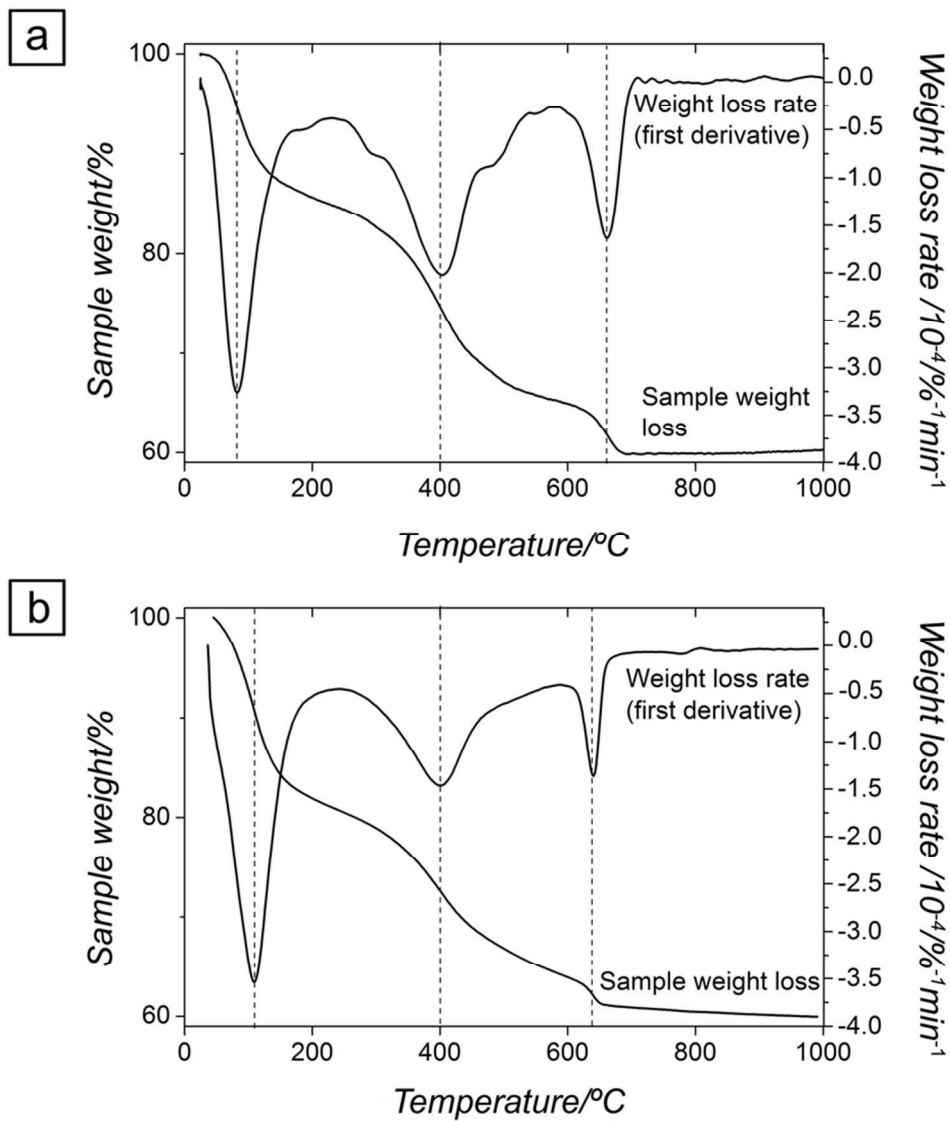
TGA (sample weight loss and weight loss rate curves) of the poorly-ordered precursor: ALC (a), ANC (b).
The curves show a progressive loss of water and the final carbonate decomposition between 450 and ~ 650
°C.
82x97mm (300 x 300 DPI)
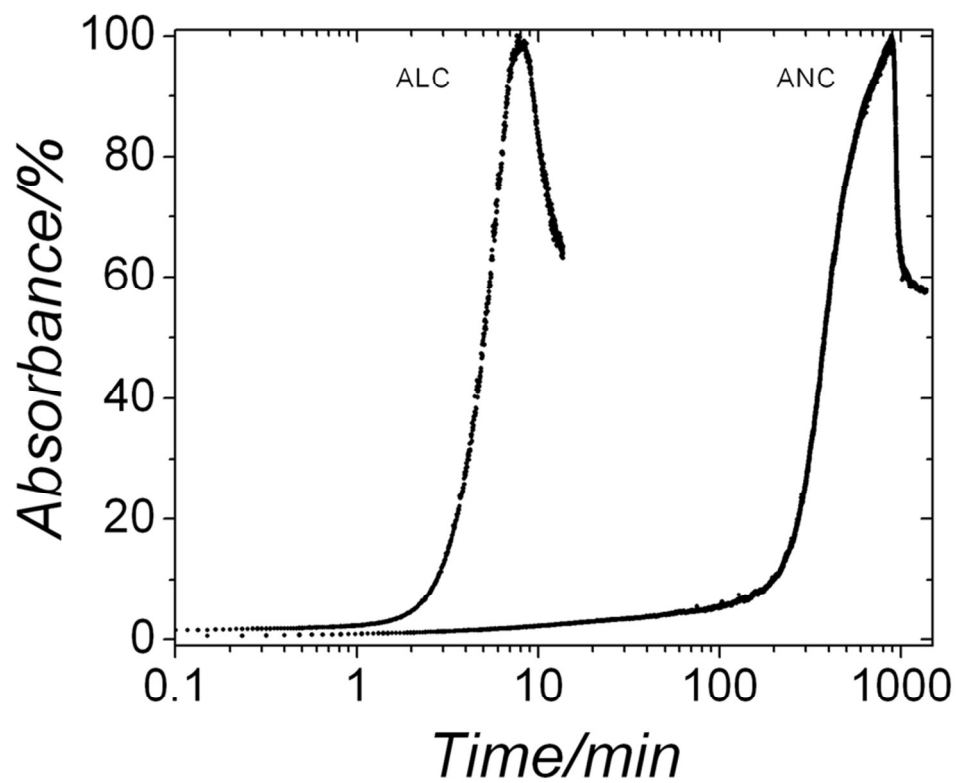
Turbidity curves from the in situ and time resolved UV-VIS experiments, showing the evolution of the crystallization of ALC and ANC in aqueous solution at ambient temperature.
82x67mm (300 x 300 DPI)
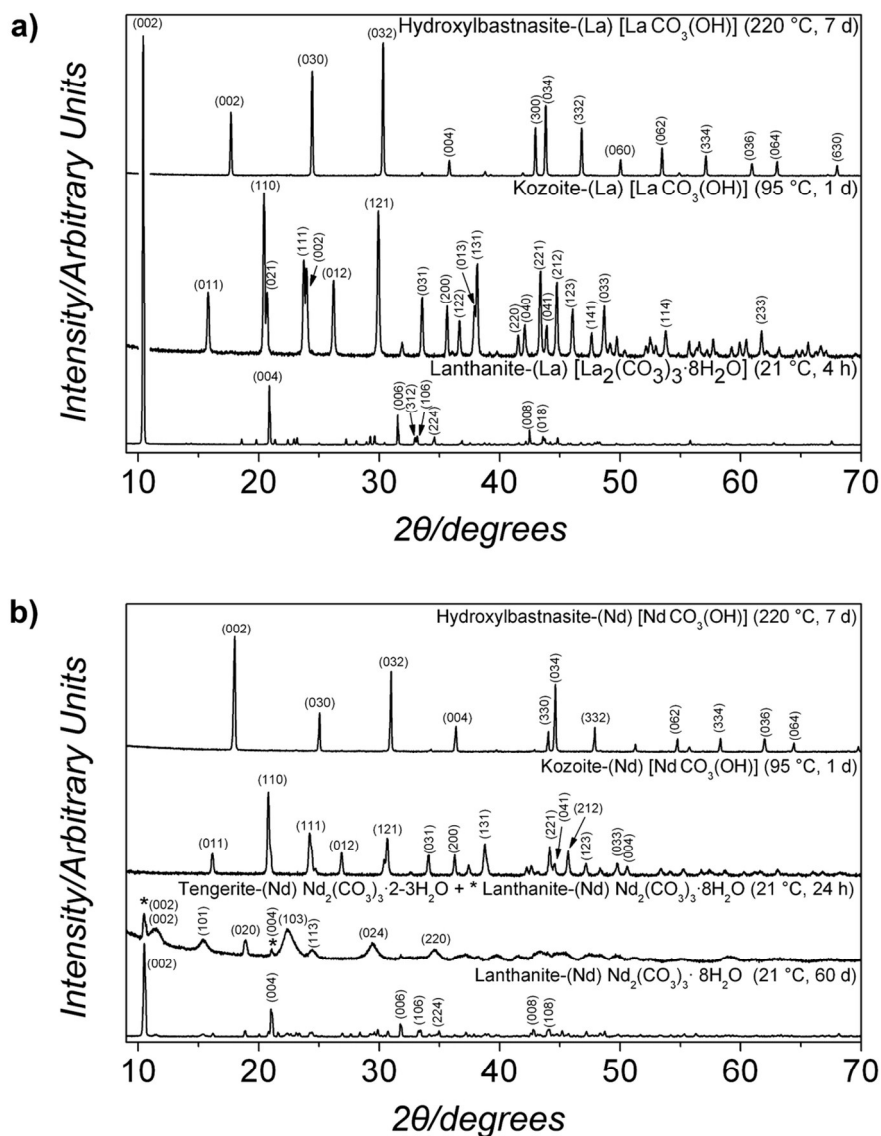
Powder X-ray diffraction patterns of the solids obtained in the (a) La and (b) Nd systems from wet-ambient conditions (21 °C) and at hydrothermal (60-220 ºC) conditions. The patterns were indexed to: (a) $La_2(CO_3)_3 \cdot 8H_2O$, kozoite-(La) $LaCO_3(OH)$ and hydroxylbastnasite-(La) $[LaCO_3(OH)]$ and (b) $Nd_2(CO_3)_3 \cdot 2\text{-}3H_2O$, $Nd_2(CO_3)_3 \cdot 8H_2O$, kozoite-(Nd) $[NdCO_3(OH)]$, hydroxylbastnasite-(Nd) $[NdCO_3(OH)]$. Full details about the indexing are presented in Fig SI-1.
106x135mm (300 x 300 DPI)
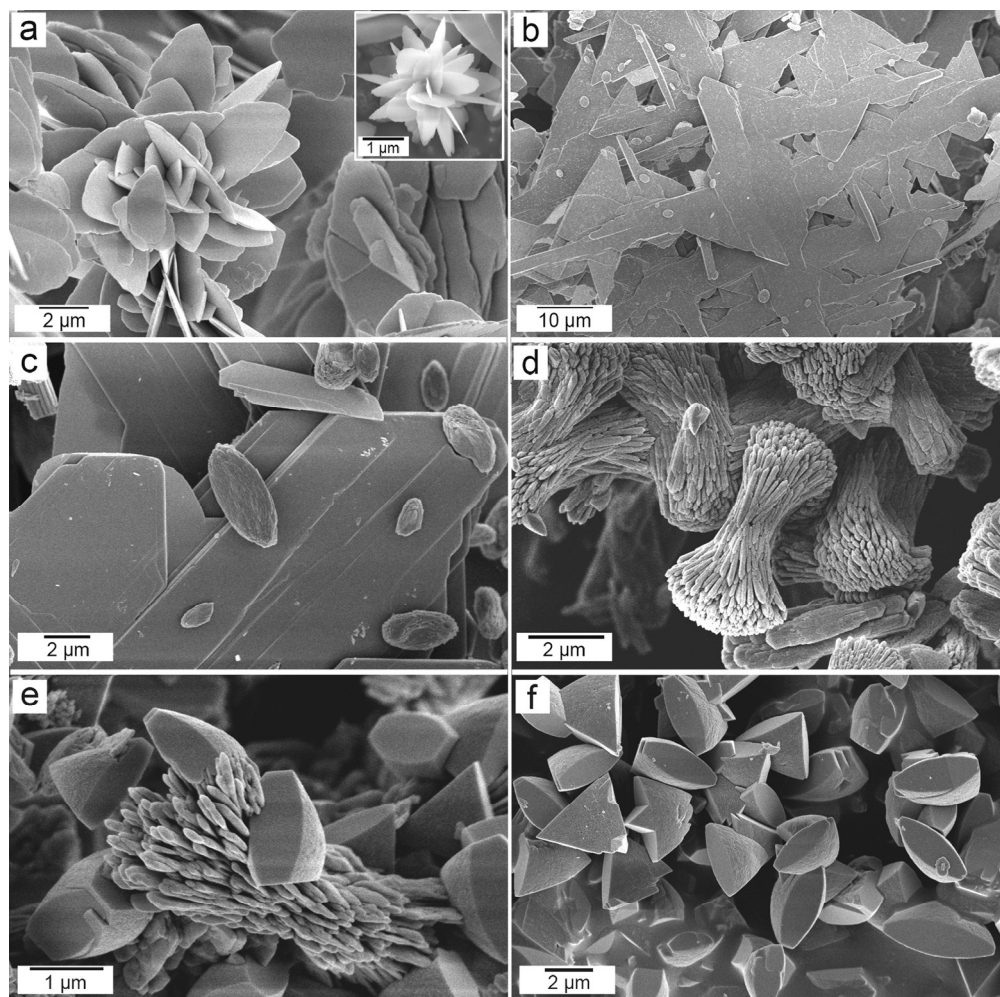
FEG-SEM images of the crystalline lanthanum end product phases of the wet-ambient and hydrothermal treatments: (a) $La_2(CO_3)_3 \cdot 8H_2O$ rosettes obtained at 21 ºC. (b) Well-faceted prisms of kozoite-(La) obtained at 21 ºC. (c) $La_2(CO_3)_3 \cdot 8H_2O$ crystals and ellipsoidal crystals of kozoite-(La) at the beginning of the transformation (d) Dumbbell-shaped kozoite-(La) obtained at 165 ºC. (e) Transformation of the dumbbell-shaped kozoite-(La) into triangular hydroxylbastnasite-(La) pyramids (f) Hydroxylbastnasite-(La) pyramids obtained as the final product of the hydrothermal treatments at 165 ºC; the same final product with the same shapes were also obtained at 220 °C.
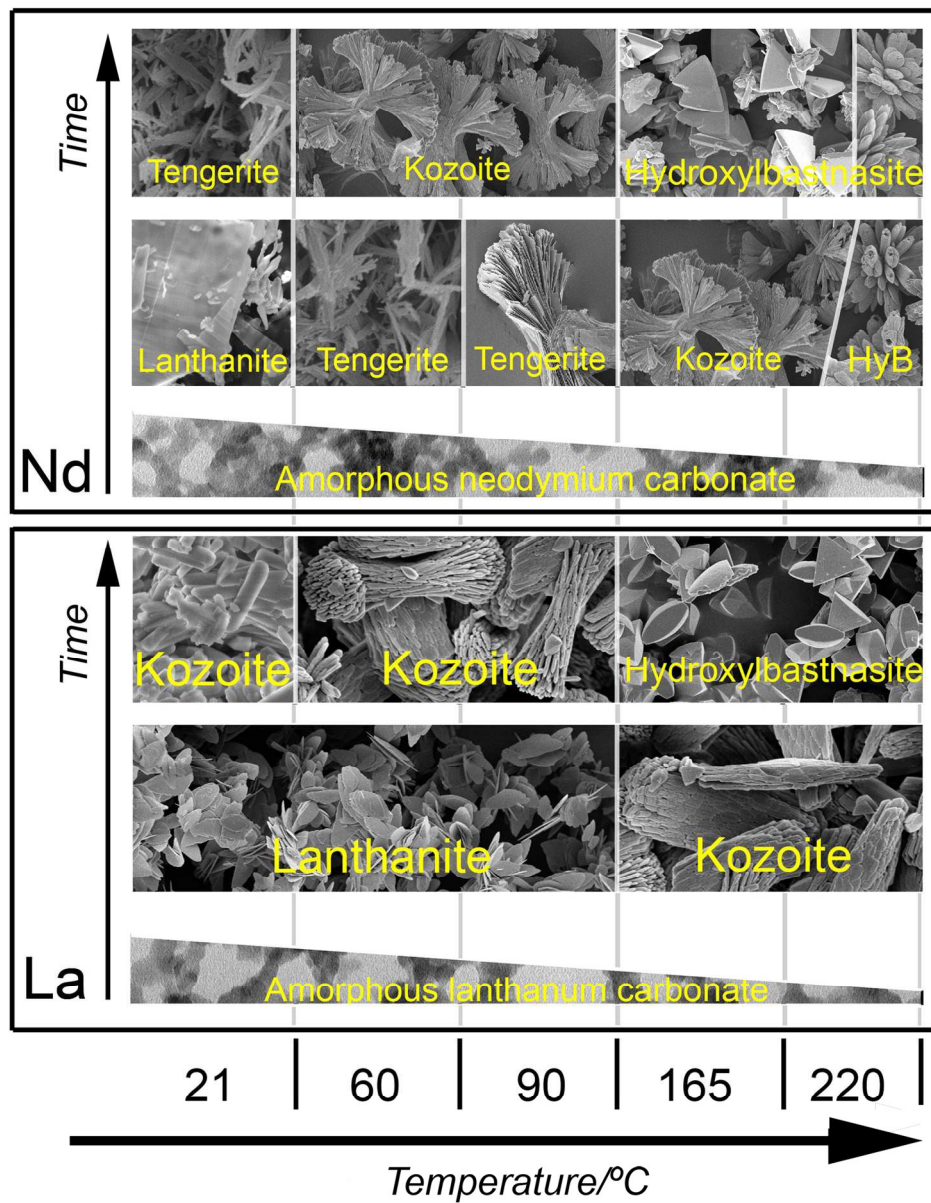
171x169mm (300 x 300 DPI)
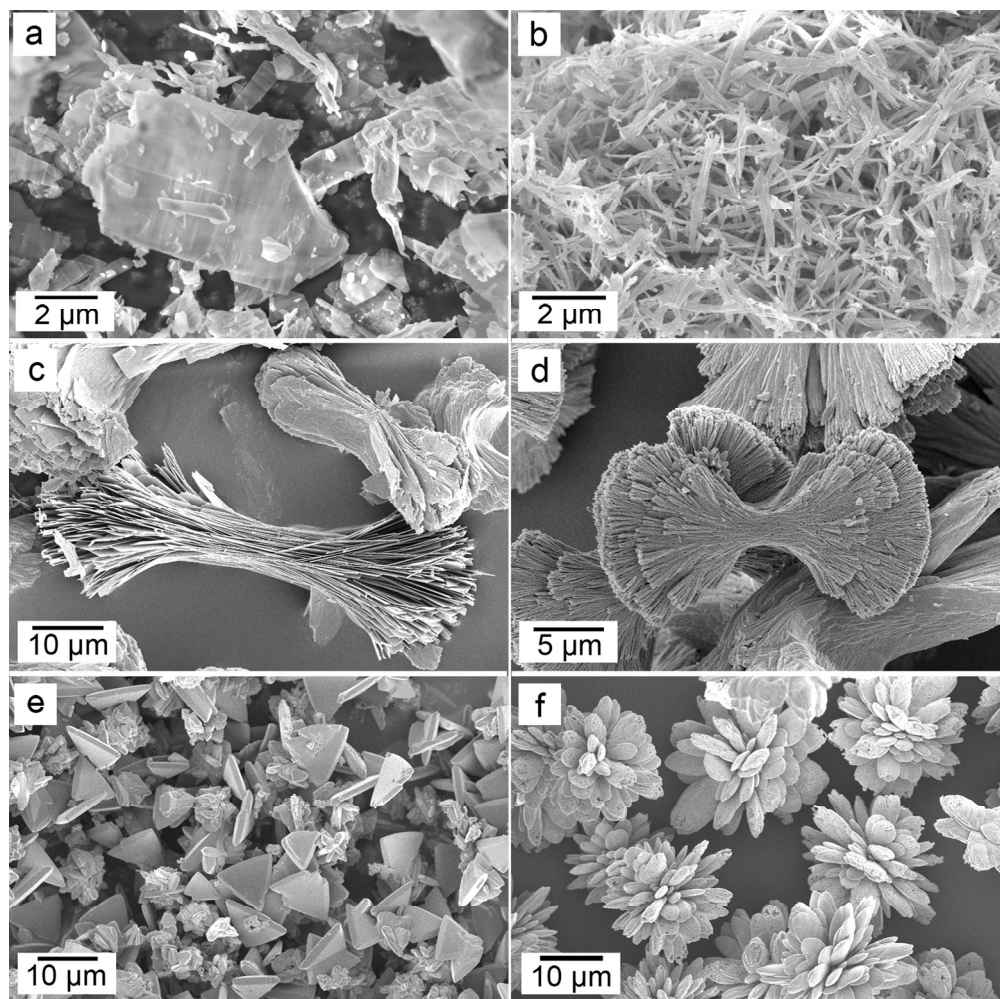
FEG-SEM images of the crystalline neodymium end product phases of the wet-ambient and hydrothermal treatments: (a) crystal plates of $Nd_2(CO_3)_3 \cdot 8H_2O$ obtained at 21 ºC. (b) Acicular needle-like crystals of tengerite-(Nd) obtained at 60 ºC. (c) Spherulitic, plate-like tengerite-(Nd) obtained at 95 ºC (d) Dumbbell-shaped kozoite-(Nd) obtained at 95 ºC. (e) Triangular hydroxylbastnasite-(Nd) pyramids obtained at 165 °C. (f) Spherulitic hydroxylbastnasite-(Nd) [$Nd(CO_3)OH$] obtained as a direct product of the transformation of the amorphous Nd carbonate precursor, ANC, at 220 ºC.

171x169mm (300 x 300 DPI)
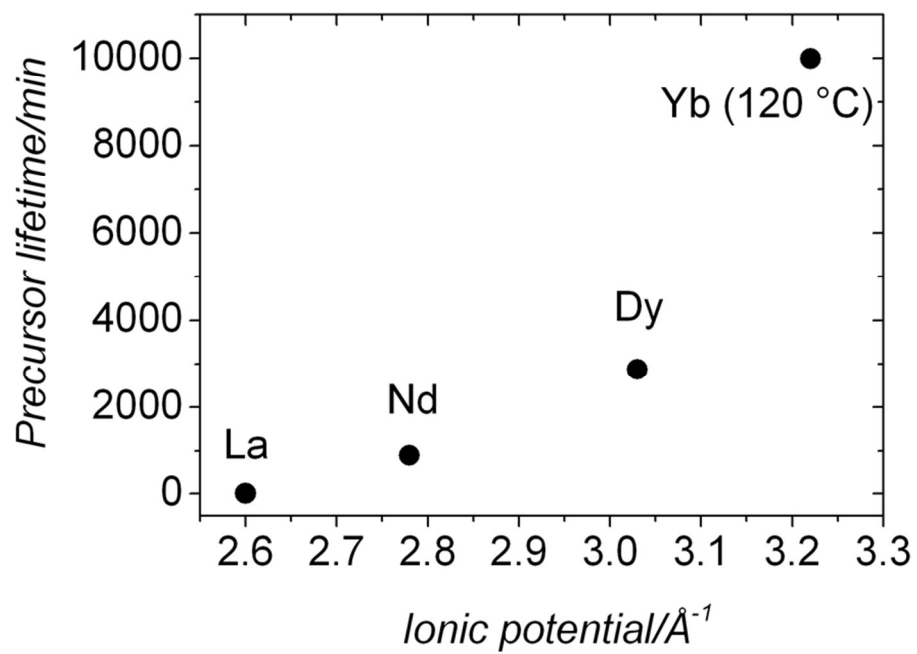
Plot showing the proportionality between the stability of the La, Nd, Dy and Yb amorphous carbonate precursors and the ionic potential of the REE^{3+} involved in the precursor.
82x57mm (300 x 300 DPI)

Summary of the crystallization products for the La and Nd systems at different temperatures in the wet-ambient and hydrothermal treatments.
171x210mm (300 x 300 DPI)